Supporting Information

Enhancing proton co-intercalation in iron ion batteries cathodes for increased capacity

Ze He,[1,2] Gao Wang,[1] Ruohan Yu,[1] Yalong Jiang,[3] Meng Huang,[4] Fangyu Xiong,[5] Shuangshuang Tan,[5] Michael F. L. De Volder,[2] Qinyou An,[1,6]*, Liqiang Mai[1,6]**

[1]Key Laboratory of Advanced Technology for Materials Synthesis and Processing, Wuhan University of Technology, Wuhan, 430070, China.

[2]Institute for Manufacturing, Department of Engineering, University of Cambridge, Cambridge CB3 0FS, UK.

[3]State Key Laboratory of New Textile Materials and Advanced Processing Technologies, Wuhan Textile University, Wuhan, 430200, China.

[4]Sanya Science and Education Innovation Park of Wuhan University of Technology, Sanya, 572000, China.

[5]College of Materials Science and Engineering, Chongqing University, Chongqing 400030, China.

[6]Hubei Longzhong Laboratory, Wuhan University of Technology (Xiangyang Demonstration Zone), Xiangyang 441000, Hubei, China.

* Corresponding Author

E-mail: mfld2@cam.ac.uk (Michael F. L. De Volder); anqinyou86@whut.edu.cn (Qinyou An); mlq518@whut.edu.cn (Liqiang Mai).

Electrochemical measurements

The electrode slurry was prepared using a formula of 70 $_{wt}$% active materials, 20 $_{wt}$% acetylene black, 10 $_{wt}$% polyvinylidene fluoride (PVDF) and an appropriate amount of N-methyl pyrrolidone (NMP). Then, the slurry was cast on carbon paper and dried in an oven at 60 ℃ for 24h. The mass loading of the FeHCF in the electrode is about 2 mg cm^{-2}. Iron foil with 0.2 mm thickness was directly used as the anodes after sanding off the surface oxide layer with sandpaper. The electrolyte contains 0.5 M $FeSO_4$ dissolved in the deionized water (purged with N_2 for 30 min to remove the dissolved O_2) and a small amount of iron powder to prevent the oxidation of the ferrous ion. Glass fiber was used as separators. Electrochemical measurements were performed in CR2016 coin cells, all the cells were assembled in the air. The cyclic voltammetry (CV) measurement was carried out from 0.2 to 1.1 V (vs Fe^{2+}/Fe) on a VMP-3 multichannel workstation. The electrochemical performance including cycling and rate performance, and galvanostatic charge/discharge (GCD) profiles of coin cells were obtained from a Neware battery system (Neware Technology Ltd.). All tests for activated FeHCF were performed after an overcharge of 16 hours at 100 mA g^{-1}.

Density functional theory calculation

All calculations were executed by the projector augmented wave (PAW)[1] method within density functional theory (DFT), conducted in the Vienna ab initio Simulation Package (VASP)[2,3]. The generalized gradient approximation (GGA) in the form of the Perdew-Burke-Ernzerhof (PBE)[4] was used to treat the exchange-correlation energy. In order to calculate the adsorption energy between H^+ and substrates (FeHCF and FeOOH), slab models with a vacuum slab of 10 Å were constructed to simulate the (200) facet of FeHCF and (130) facet of FeOOH. A kinetic energy cutoff of 500 eV was used for wave functions expanded in the plane wave basis. Besides, spin polarization was considered. The energy (converged to 1.0×10^{-6} eV $atom^{-1}$) and force (converged to 0.05 eV $Å^{-1}$) were set as the convergence criterion for geometry optimization. For the Brillouin-zone sampling, 4×4×4 k-points mesh were adopted to ensure convergence of the total energy.

The adsorption energy (ΔE_{H^+}) were determined by the following formula:

$$\Delta E_{H^+} = E_{sub+H^+} - E_{sub} - E_{H^+}$$

where $E_{\mathrm{sub}+H^+}$ is the total energy of H^+ adsorbed on different substrates, E_{sub} and E_{H^+} are the energy of the pure substrates and the single H^+.

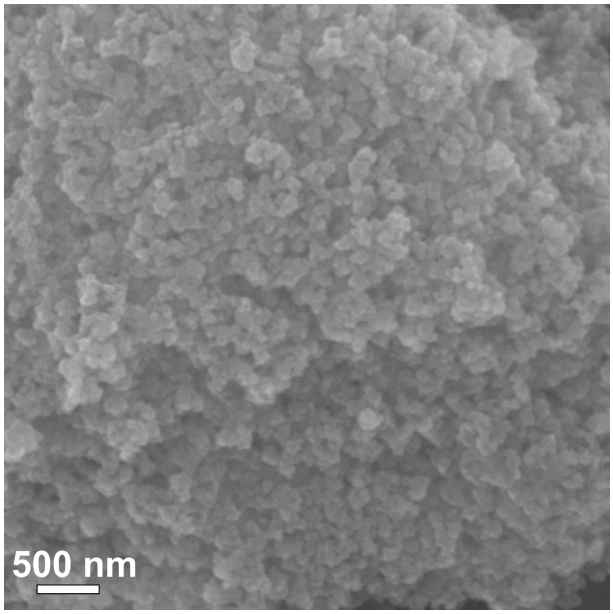

Figure S1. Scanning Electron Microscope (SEM) image of the as-prepared FeHCF cathode.

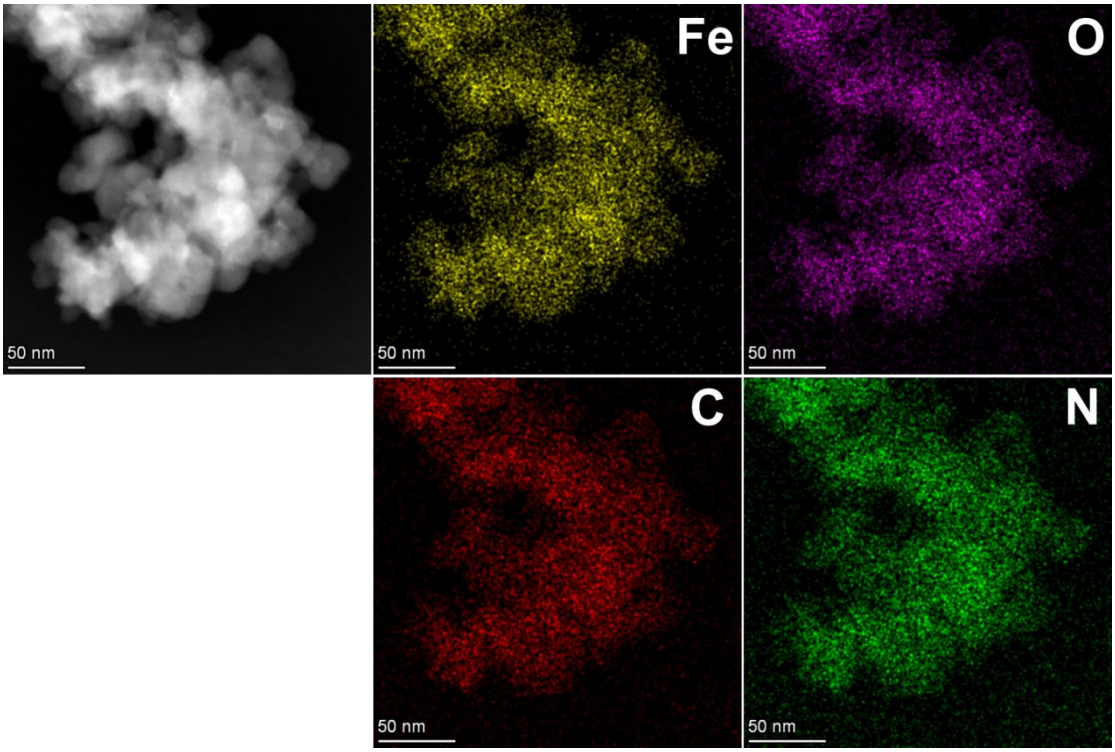

Figure S2. Transmission Electron Microscopy (TEM) Energy-Dispersive X-ray Spectroscopy (EDS) elemental mapping analysis of the FeHCF cathode. Which show that the Fe, C, N and O elements are homogeneously distributed in the sample.

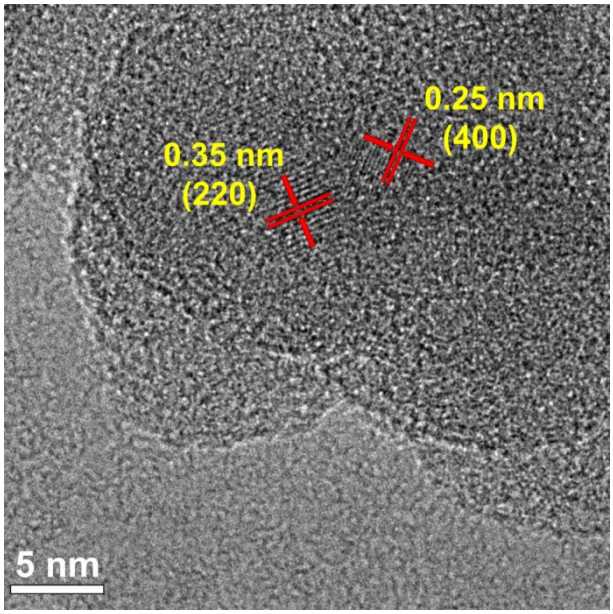

Figure S3. The High-Resolution Transmission Electron Microscopy (HRTEM) image of the FeHCF cathode. The diffraction fringes observed in the HRTEM image correspond to the interlayer spacing of 0.35 nm and 0.25 nm, which can be attributed to the (220) and (400) crystallographic planes of FeHCF, respectively.

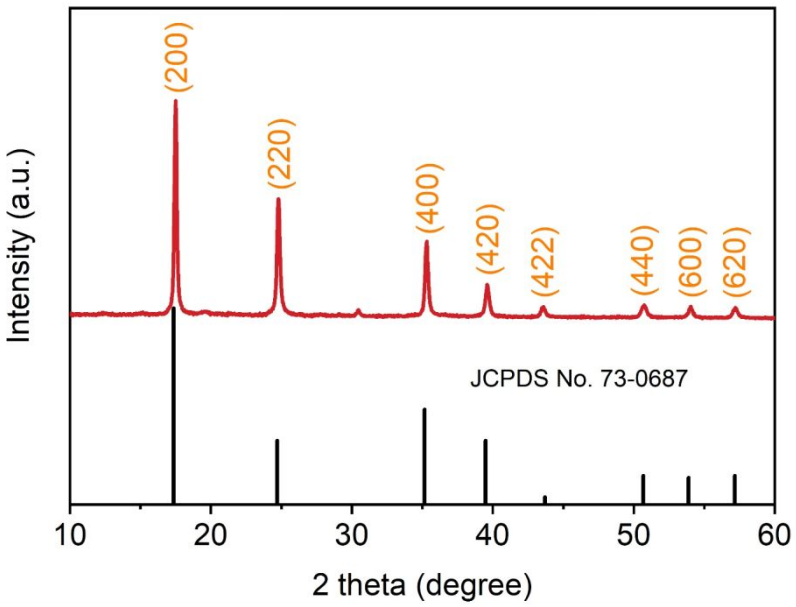

Figure S4. The X-ray Diffraction (XRD) patterns of the FeHCF powder. The diffraction peaks at approximately 17.53˚, 24.8˚, 35.3˚, 39.6˚, 43.6˚, 50.7˚, 54.0˚, 57.2˚, corresponding to the (200), (220), (400), (420), (440), (600) and (620) lattice planes (JCPDS No. 73-0689).

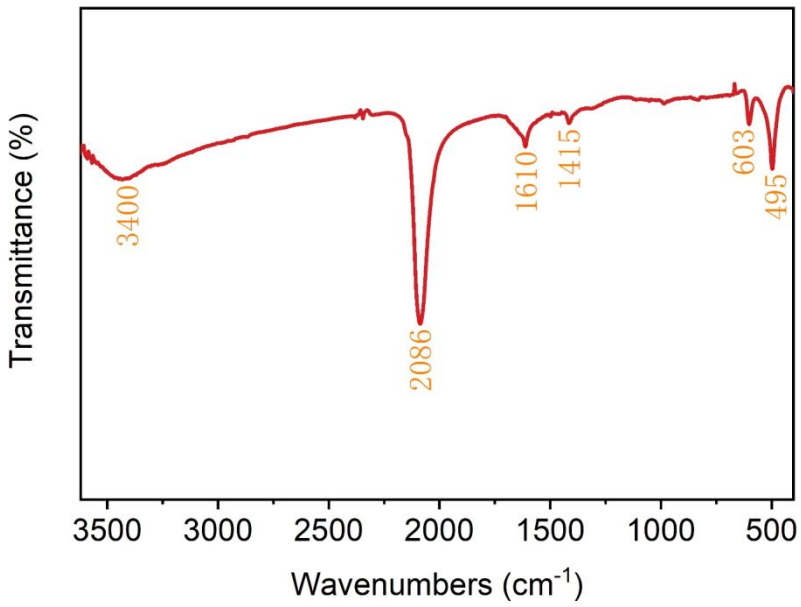

Figure S5. Fourier Transform Infrared (FT-IR) spectrum of the FeHCF sample. The absorption peaks at 495, 603 and 2086 cm^{-1} corresponding to the vibrations of Fe-O, Fe-CN and C≡N chemical bonds, revealing the metal-organic compound structure. Furthermore, the absorption peaks at 1610 and 3400 cm^{-1} are attributed to the stretching and in-plane deformation of O-H, indicating the presence of crystal water in the FeHCF crystal.

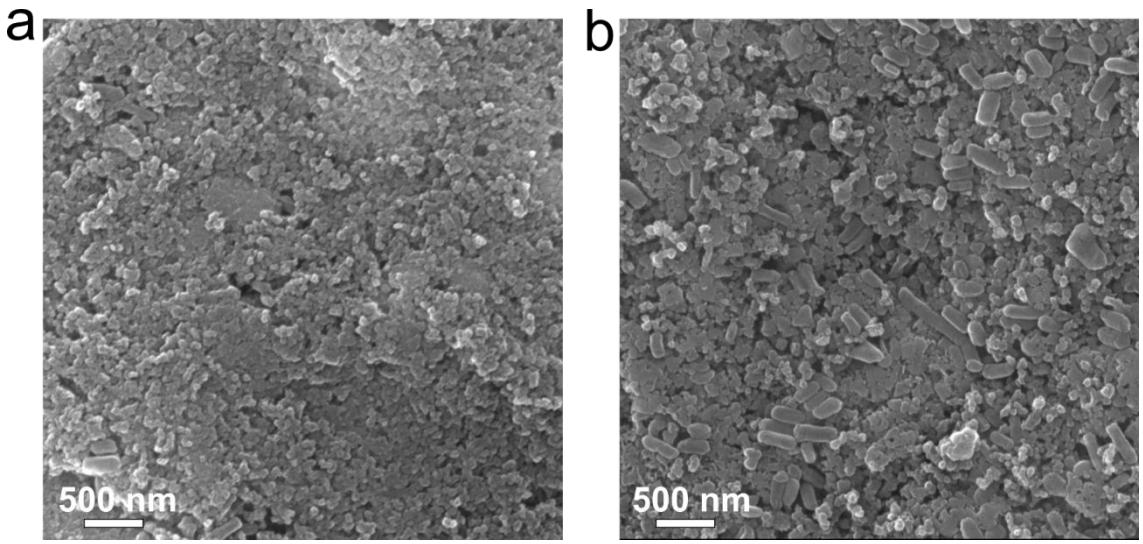

Figure S6. Ex-situ SEM images of (a) the pristine FeHCF electrode and (b) the un-activated FeHCF electrode after the first charge.

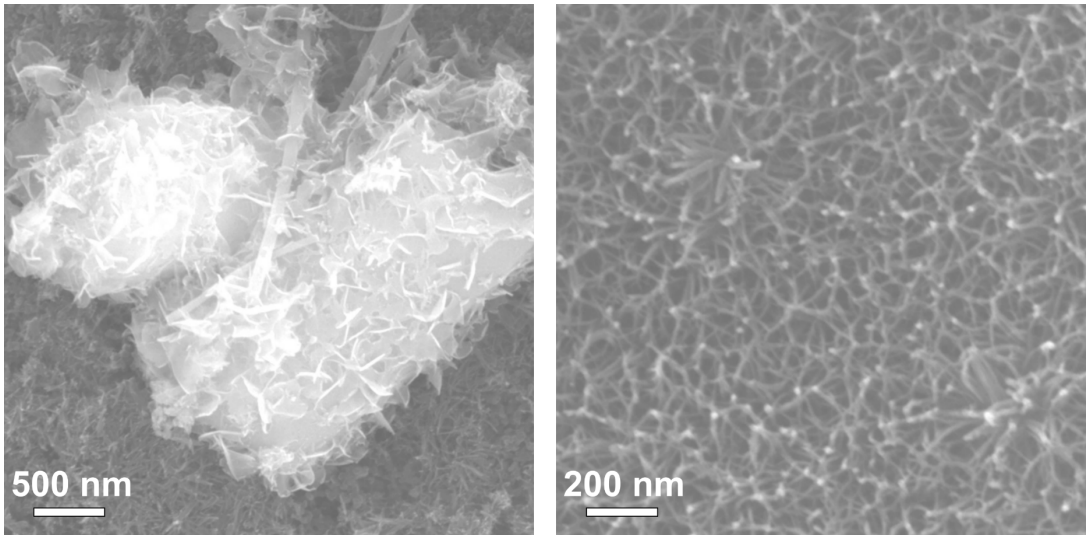

Figure S7. SEM images of the surface of the activated FeHCF electrode after discharge. The images show the coexistence of FeOOH nanowire network and $Fe_3(SO_4)_2(OH)_2$ micro-flower on the surface of the discharged activated-FeHCF electrode.

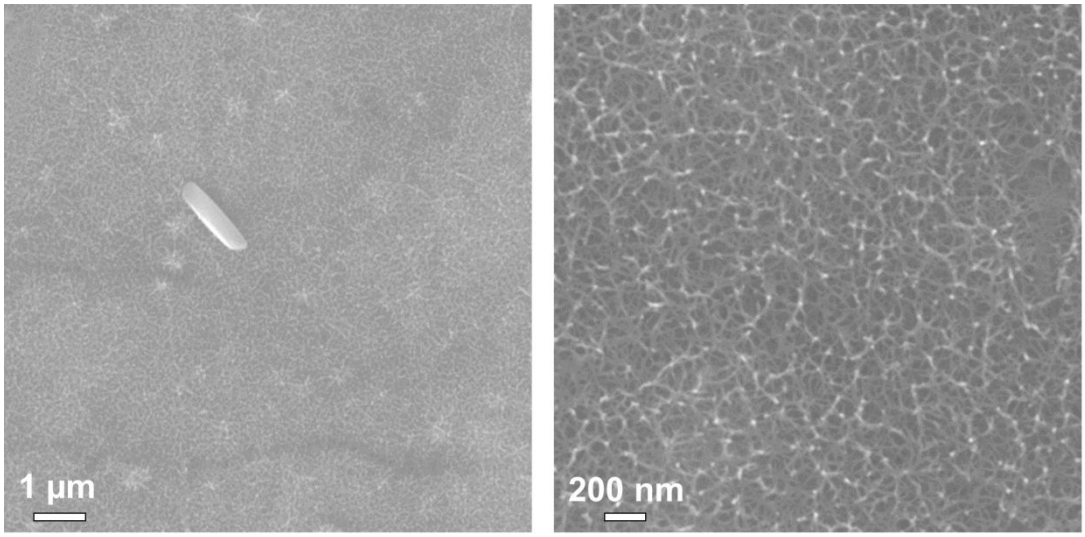

Figure S8. SEM images of the surface of the activated FeHCF electrode after charge.

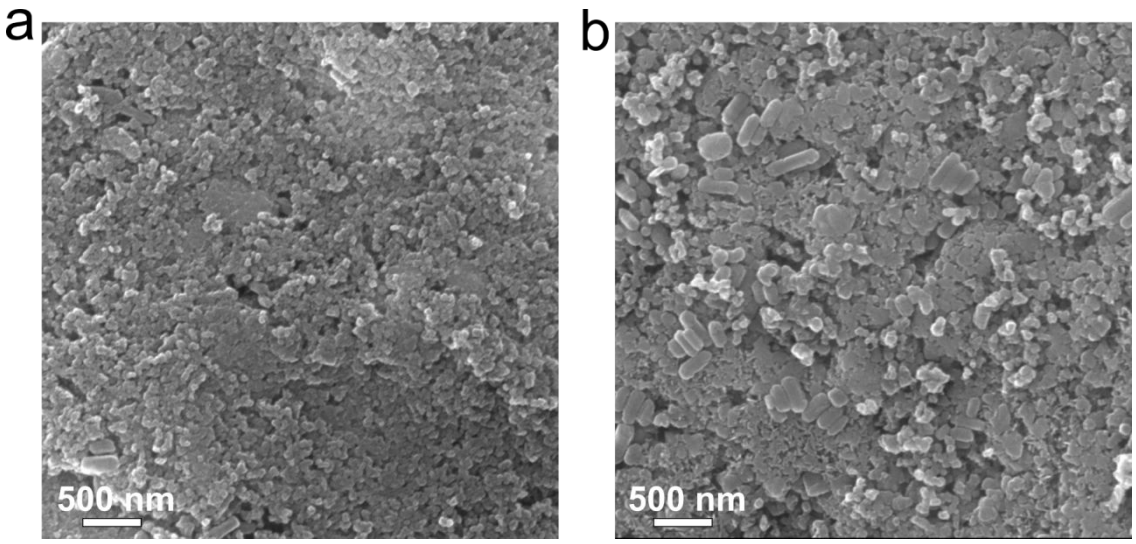

Figure S9. Ex-situ SEM images of (a) the pristine FeHCF electrode and (b) the un-activated FeHCF electrode after discharge.

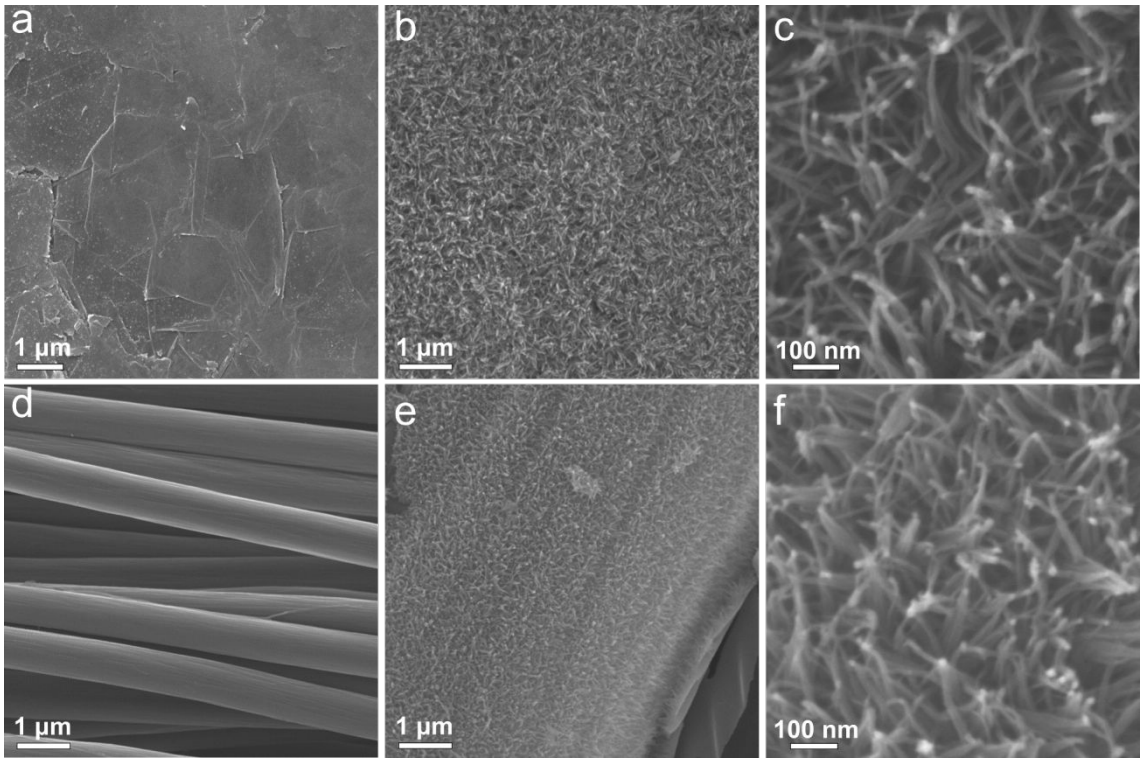

Figure S10. Ex-situ SEM images of (a) the pristine carbon paper (CP), (d) carbon cloth (CC), and the over-charged (b-c) CP and (e-f) CC.

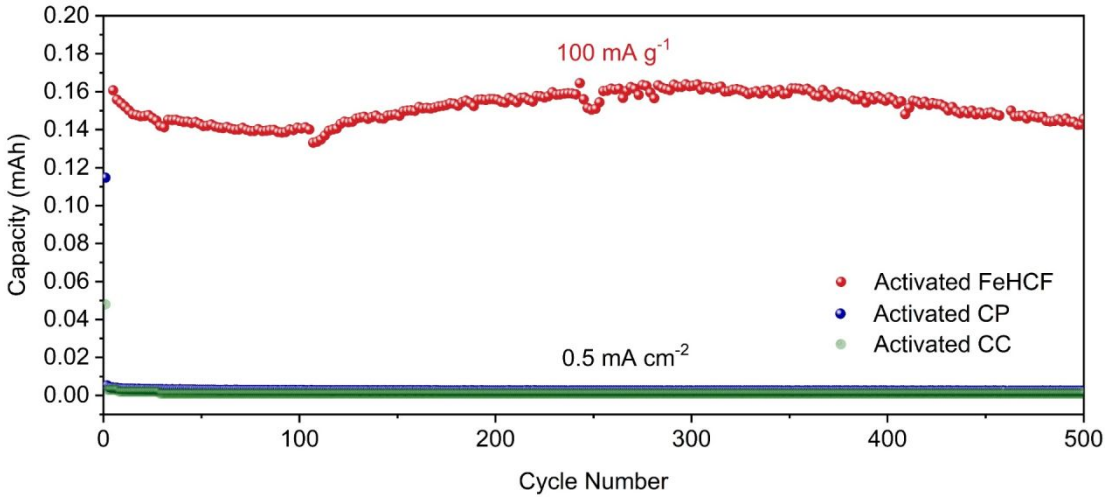

Figure S11. Capacity comparison of the activated FeHCF, CP, and CC.

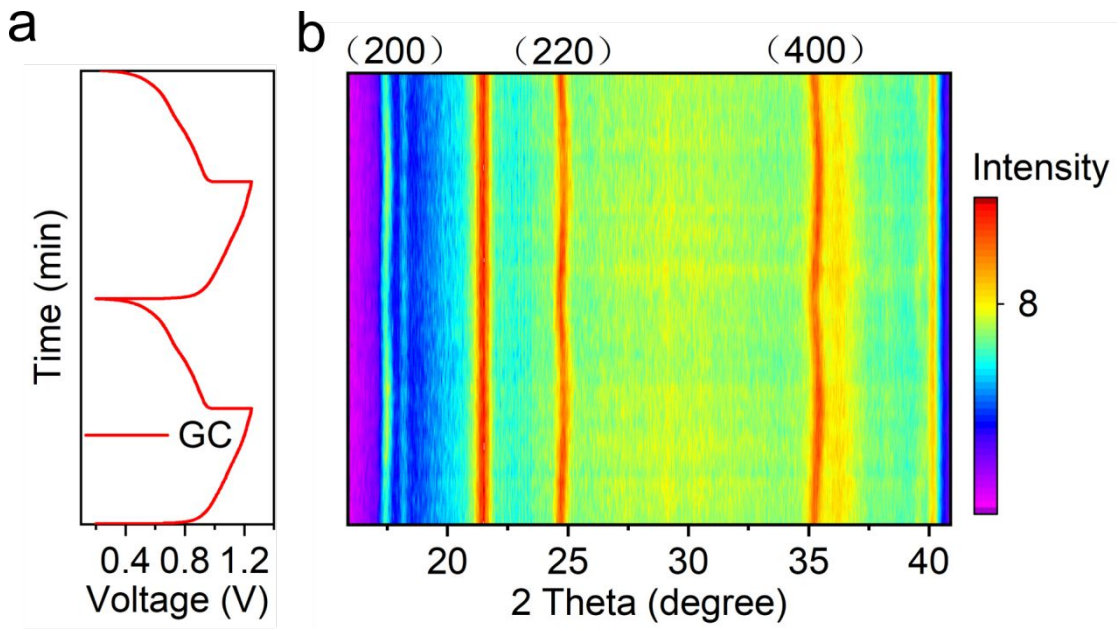

Figure S12. In-situ XRD characterization and the corresponding GCD potential profiles of pristine FeHCF.

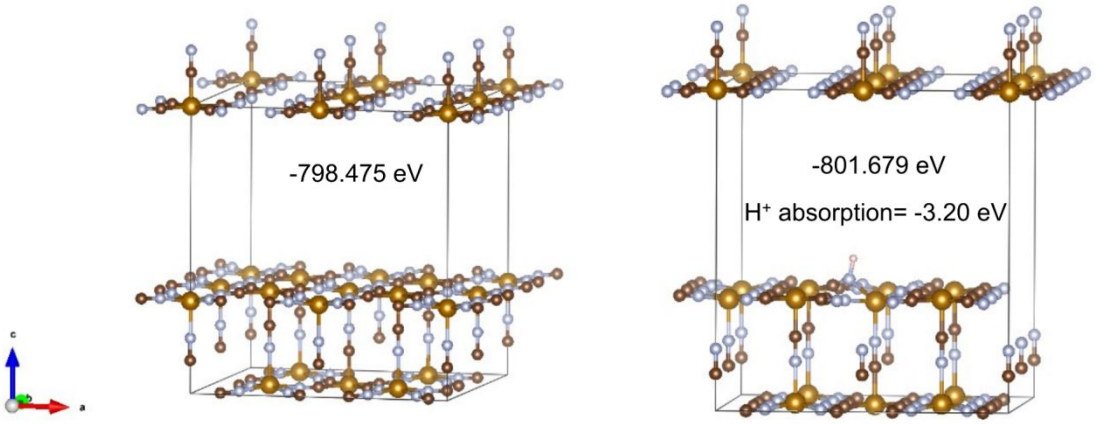

Figure S13. DFT calculation for the H^+ absorption energy of the FeHCF cathode.

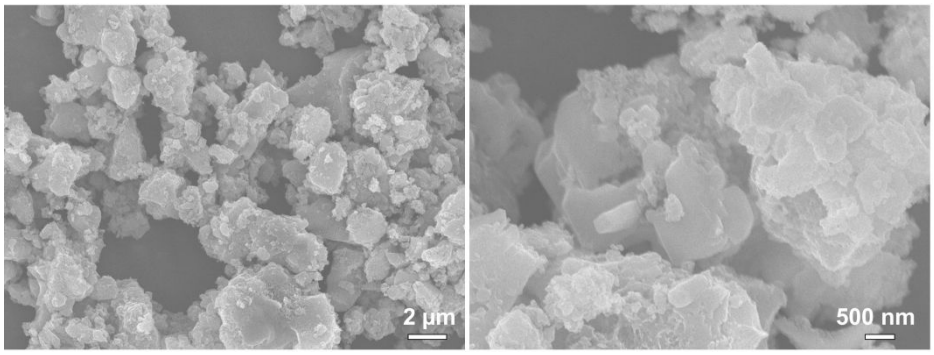

Figure S14. SEM images of the NFPP cathode.

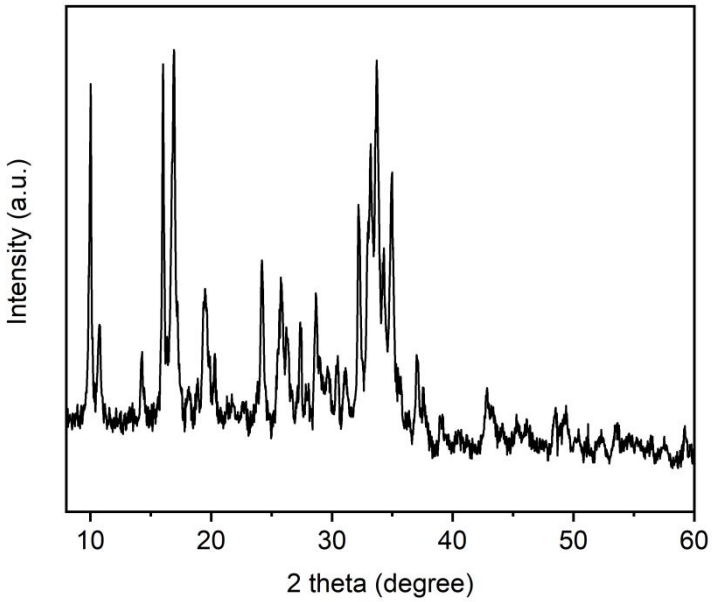

Figure S15. XRD pattern of the synthesized $Na_4Fe_3(PO_4)_2P_2O_7$ (NFPP) cathode.

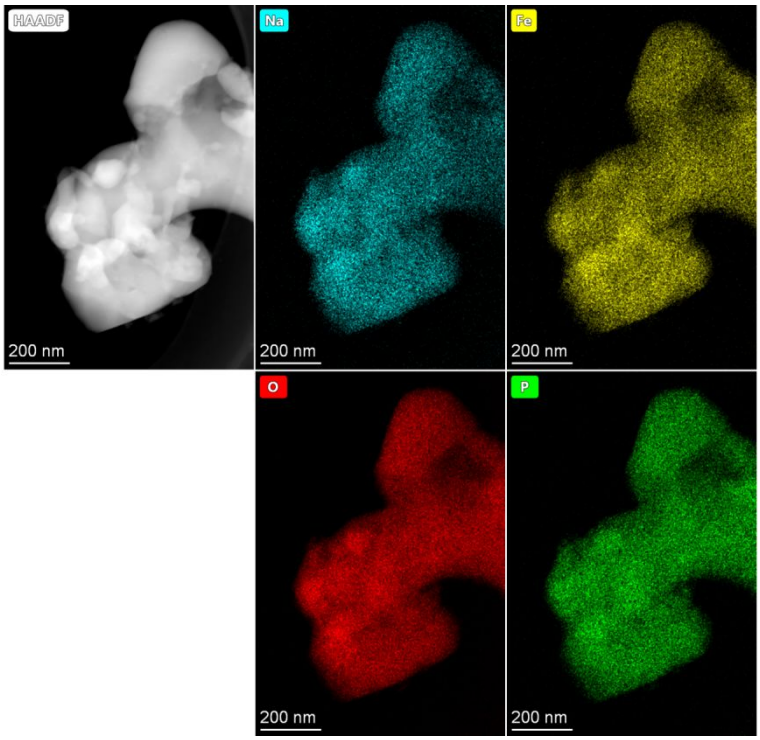

Figure S16. EDS-HAADF elemental mappings of the NFPP cathode.

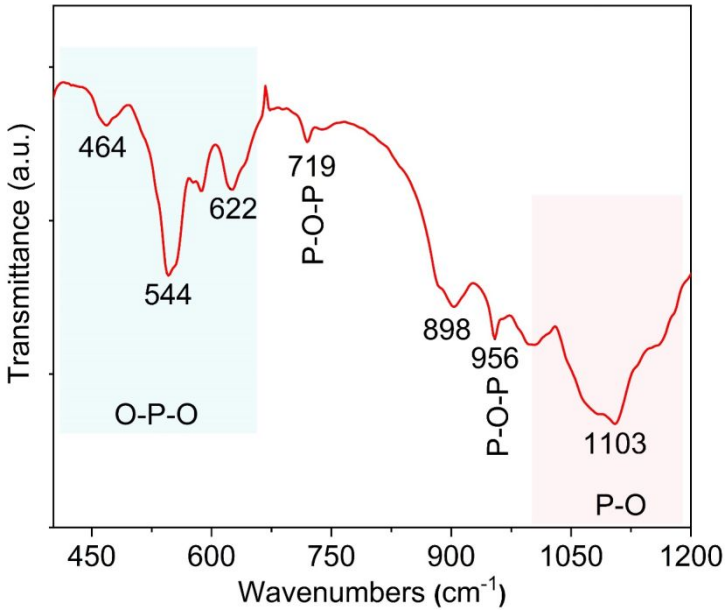

Figure S17. The Fourier transform infrared (FT-IR) spectra of the NFPP cathode.

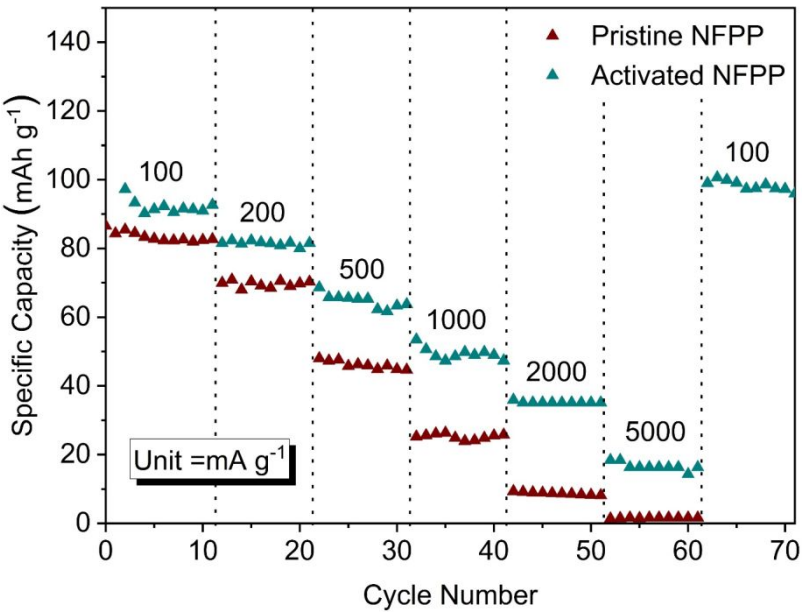

Figure S18. Rate performance of the pristine and activated NFPP cathodes.

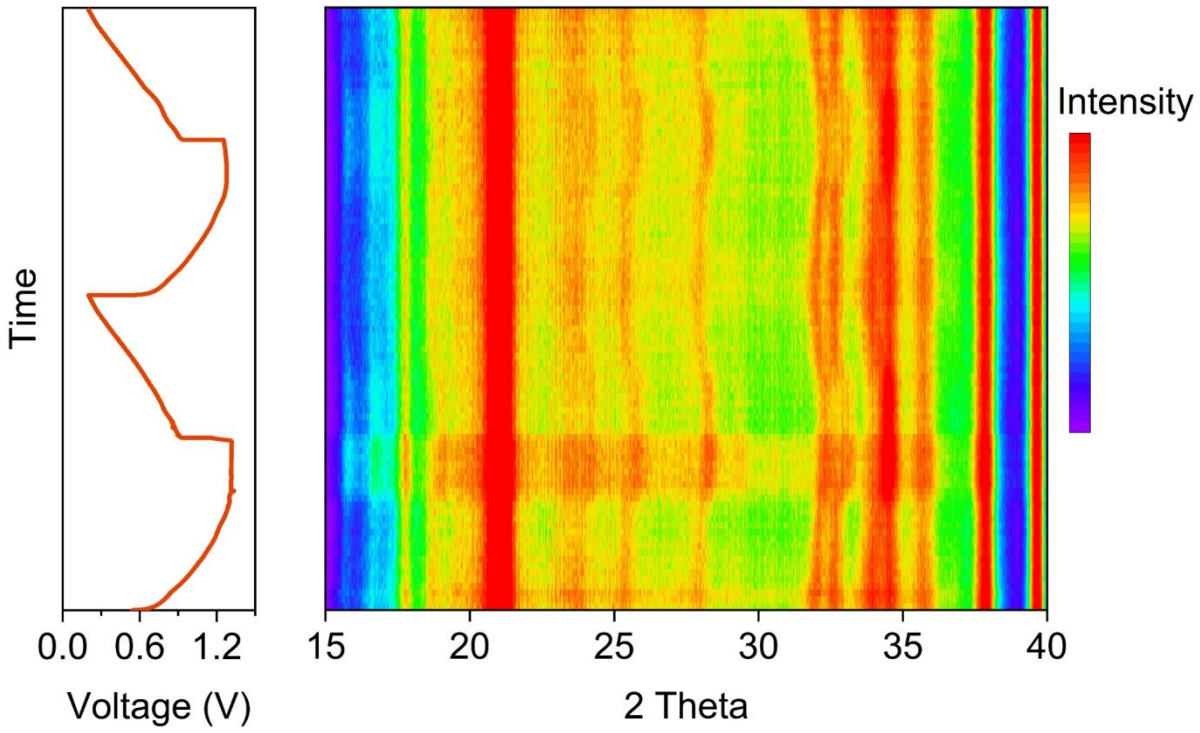

Figure S19. In-situ XRD characterization and the corresponding GCD curves of the activated NFPP cathode.

Table S1. Composition Results of (1) Spectrum of EELS Spectrum Image

Element	**Shell**	**Signal (Counts)**	**Comp. (at.%)**	**Rel. comp. (/O)**	**X-section (barns)**	**X-section Model**
O	K	$3.5*10^5 \pm 1.5*10^3$	66.5	1.0	1792.3± 89.6	Hartree-Slater
Fe	L	$4.7*10^5 \pm 1.3*10^3$	33.5	0.5	4708.1± 470.8	Hartree-Slater

Table S2. PBAs cathodes for aqueous multivalent ions batteries

Cathode	**Charge carrier**	**Current density**	**Specific capacity**	**Ref.**
FeHCF	Fe^{2+}	60 mA g^{-1}	60 mAh g^{-1}	5
Mg-doped FeHCF	Fe^{2+}	100 mA g^{-1}	91 mAh g^{-1}	6
Activated FeHCF	Fe^{2+}	100 mA g^{-1}	151 mAh g^{-1}	This work
NiHCF	Mg^{2+}	~250 mA g^{-1}	~50 mAh g^{-1}	7
CuHCF	Mg^{2+}	100 mA g^{-1}	50 mAh g^{-1}	8
NiHCF	Mg^{2+}	100 mA g^{-1}	65 mAh g^{-1}	9
CuHCF	Ca^{2+}	~250 mA g^{-1}	45 mAh g^{-1}	10
CuHCF	Ca^{2+}	300 mA g^{-1}	50 mAh g^{-1}	11
CuHCF	Ca^{2+}	~17 mA g^{-1}	85 mAh g^{-1}	12
CuHCF	Al^{3+}	50 mA g^{-1}	62 mAh g^{-1}	13
CoHCF	Al^{3+}	100 mA g^{-1}	50 mAh g^{-1}	14
NiHCF	Al^{3+}	20 mA g^{-1}	45 mAh g^{-1}	15

(1) Kresse, G.; Joubert, D. From Ultrasoft Pseudopotentials to the Projector Augmented-Wave Method. *Phys. Rev. B* **1999**, *59*, 1758–1775.
(2) Kresse, G.; Furthmüller, J. Efficient Iterative Schemes for Ab Initio Total-Energy Calculations Using a Plane-Wave Basis Set. *Phys. Rev. B* **1996**, *54*, 11169–11186.
(3) Kresse, G.; Furthmüller, J. Efficiency of Ab-Initio Total Energy Calculations for Metals and Semiconductors Using a Plane-Wave Basis Set. *Comput. Mater. Sci.* **1996**, *6*, 15–50.
(4) Perdew, J. P.; Burke, K.; Ernzerhof, M. Generalized Gradient Approximation Made Simple. *Phys. Rev. Lett.* **1996**, *77*, 3865–3868.
(5) Wu, X.; Markir, A.; Xu, Y.; Zhang, C.; Leonard, D. P.; Shin, W.; Ji, X. A Rechargeable Battery with an Iron Metal Anode. *Adv. Funct. Mater.* **2019**, *29*, 1900911.
(6) Huang, G.; Lao, Z.; He, Z.; Xiong, F.; Tan, S.; Huang, M.; Thompson, G.; An, Q.; Mai, L. Mg-Substituted Prussian Blue as a Low-Strain Cathode Material for Aqueous Fe-Ion Batteries. *Chem. Commun.* **2023**, *59*, 4067–4070.
(7) Wang, R. Y.; Wessells, C. D.; Huggins, R. A.; Cui, Y. Highly Reversible Open Framework Nanoscale Electrodes for Divalent Ion Batteries. *Nano Lett.* **2013**, *13*, 5748–5752.
(8) Mizuno, Y.; Okubo, M.; Hosono, E.; Kudo, T.; Oh-ishi, K.; Okazawa, A.; Kojima, N.; Kurono, R.; Nishimura, S.; Yamada, A. Electrochemical Mg2+ Intercalation into a Bimetallic CuFe Prussian Blue Analog in Aqueous Electrolytes. *J. Mater. Chem. A* **2013**, *1*, 13055–13059.
(9) Chen, L.; Bao, J. L.; Dong, X.; Truhlar, D. G.; Wang, Y.; Wang, C.; Xia, Y. Aqueous Mg-Ion Battery Based on Polyimide Anode and Prussian Blue Cathode. *ACS Energy Lett.* **2017**, *2*, 1115–1121.
(10) Gheytani, S.; Liang, Y.; Wu, F.; Jing, Y.; Dong, H.; Rao, K. K.; Chi, X.; Fang, F.; Yao, Y. An Aqueous Ca-Ion Battery. *Adv. Sci.* **2017**, *4*, 1700465.
(11) Adil, Md.; Sarkar, A.; Roy, A.; Panda, M. R.; Nagendra, A.; Mitra, S. Practical Aqueous Calcium-Ion Battery Full-Cells for Future Stationary Storage. *ACS Appl. Mater. Interfaces* **2020**, *12*, 11489–11503.
(12) Lee, C.; Jeong, S.-K. Modulating the Hydration Number of Calcium Ions by Varying the Electrolyte Concentration: Electrochemical Performance in a Prussian Blue Electrode/Aqueous Electrolyte System for Calcium-Ion Batteries. *Electrochimica Acta* **2018**, *265*, 430–436.
(13) Liu, S.; Pan, G. L.; Li, G. R.; Gao, X. P. Copper Hexacyanoferrate Nanoparticles as Cathode Material for Aqueous Al-Ion Batteries. *J. Mater. Chem. A* **2014**, *3*, 959–962.
(14) Ru, Y.; Zheng, S.; Xue, H.; Pang, H. Potassium Cobalt Hexacyanoferrate Nanocubic Assemblies for High-Performance Aqueous Aluminum Ion Batteries. *Chem. Eng. J.* **2020**, *382*, 122853.
(15) Gao, Y.; Yang, H.; Wang, X.; Bai, Y.; Zhu, N.; Guo, S.; Suo, L.; Li, H.; Xu, H.; Wu, C. The Compensation Effect Mechanism of Fe–Ni Mixed Prussian Blue Analogues in Aqueous Rechargeable Aluminum-Ion Batteries. *ChemSusChem* **2020**, *13*, 732–740.